Article

Physical properties of asteroid Dimorphos as derived from the DART impact

S. D. Raducan [1] ✉, M. Jutzi [1], A. F. Cheng [2], Y. Zhang [3], O. Barnouin [2], G. S. Collins [4], R. T. Daly [2], T. M. Davison [4], C. M. Ernst [2], T. L. Farnham [3], F. Ferrari [5], M. Hirabayashi [6,7], K. M. Kumamoto [8], P. Michel [9,10], N. Murdoch [11], R. Nakano [6,7], M. Pajola [12], A. Rossi [13], H. F. Agrusa [3,9], B. W. Barbee [14], M. Bruck Syal[8], N. L. Chabot [2], E. Dotto [15], E. G. Fahnestock [16], P. H. Hasselmann[15], I. Herreros [17], S. Ivanovski[18], J. -Y. Li [19], A. Lucchetti [12], R. Luther [20], J. Ormö [17], M. Owen [8], P. Pravec[21], A. S. Rivkin [2], C. Q. Robin[11], P. Sánchez [22], F. Tusberti [12], K. Wünnemann [20], A. Zinzi [23], E. Mazzotta Epifani [15], C. Manzoni [24] & B. H. May[24]

On 26 September 2022, NASA's Double Asteroid Redirection Test (DART) mission successfully impacted Dimorphos, the natural satellite of the binary near-Earth asteroid (65803) Didymos. Numerical simulations of the impact provide a means to find the surface material properties and structures of the target that are consistent with the observed momentum deflection efficiency, ejecta cone geometry and ejected mass. Our simulation that best matches the observations indicates that Dimorphos is weak, with a cohesive strength of less than a few pascals, like asteroids (162173) Ryugu and (101955) Bennu. We find that the bulk density of Dimorphos ρ_B is lower than ~2,400 kg m^{-3} and that it has a low volume fraction of boulders (≲40 vol%) on the surface and in the shallow subsurface, which are consistent with data measured by the DART experiment. These findings suggest that Dimorphos is a rubble pile that might have formed through rotational mass shedding and reaccumulation from Didymos. Our simulations indicate that the DART impact caused global deformation and resurfacing of Dimorphos. ESA's upcoming Hera mission may find a reshaped asteroid rather than a well-defined crater.

Double Asteroid Redirection Test (DART) was a planetary defence mission to demonstrate the feasibility of using a kinetic impactor to change the trajectory of an asteroid[1]. The impact was successful and highly effective, resulting in a reduction in Dimorphos's orbital period around Didymos, which was initially 11 h and 55 min, by 33 ± 1 min (ref. 2). The LICIACube Unit Key Explorer (LUKE) instrument onboard the cubesat[3] captured images of the system between 29 and 320 s after impact to reveal filamentary streams of ejecta and other complex patterns that expanded for several kilometres from the impact site[4]. Moreover, the dramatic brightening of the Didymos system by solar illumination of released impact ejecta was observed by ground- and space-based telescopes[2,5,6] for many weeks after the impact.

The obtained 33 min reduction in the binary orbital period[2] implies a momentum transfer to Dimorphos that exceeded the incident momentum of the DART spacecraft by a factor β that ranges from 2.2 to 4.9 depending on the mass of Dimorphos[7], which is not currently known but will be measured by the ESA Hera spacecraft in early 2027[8]. The β parameter is defined as the ratio of the target momentum increment after the impact to the impactor momentum, in the direction of the net ejecta momentum, and is related to the additional thrust from the

production of impact ejecta[7,9]. β strongly depends on impact conditions (impact velocity and impact angle[1]) and target material properties, such as strength, porosity, bulk density and target surface structure[10–12].

Information about the spacecraft, the impact location and the impact angle are well understood for the DART impact[1] (Extended Data Fig. 1 and Extended Data Table 1). However, the mass and surface properties of Dimorphos are still ambiguous. It was not possible to directly measure the mass and bulk density of Dimorphos with DART or LICIACube. Instead, these parameters were estimated from the total mass of the binary system, as derived from Dimorphos's orbit[13], and updated volume estimates of Didymos and Dimorphos provided by DART (ref. [1]). The estimated bulk density of Dimorphos ranges from $\rho_B = 1{,}500$ to $3{,}300$ kg m^{-3} (refs. [1,7]).

The surface material properties and subsurface structure of Dimorphos were also not directly measured. However, these target parameters are vital for understanding the impact process and for transforming the kinetic impactor method from a full-scale experiment by DART into a well-understood and reliable mitigation technique for planetary defence. Moreover, the material properties of Dimorphos provide information about the origin and evolution of the Didymos–Dimorphos system as well as the overall characteristics of rubble-pile asteroids and binary asteroid systems.

In this work, we simulate the DART impact numerically and compare the results with observations to infer the properties of Dimorphos. We performed numerical simulations of the DART impact using the shock physics code Bern SPH (refs. [14,15]) over a range of assumed sets of material properties and interior structures for Dimorphos. We represented the DART spacecraft as a low-density spherical projectile of equivalent mass ('Projectile' section in Methods) while the impact velocity and angle were kept fixed. We simulated the asteroid's response to the DART impact for up to 1 h after the time of impact using the numerical approach developed in refs. [16,17] to model a late-stage, low-speed deformation ('Modelling approach for the late-stage evolution' in Methods). Bern SPH's fast-integration scheme has been validated against laboratory experiments[18] and was recently successfully applied to model the impact of the Hayabusa2 Small Carry-on Impactor[17]. Due to the relatively short timescales modelled, the rotation of Dimorphos around Didymos's and Didymos's gravity were not accounted for.

We obtained realistic configurations of boulders for our rubble-pile targets from simulations of the gravitational collapse of a cloud of spherical particles with a predefined size–frequency distribution (SFD)[1,19]. To closely replicate the topography described by ref. [1], we then selectively removed particles positioned near the surface.

To explore a large possible range of boulder volume fractions (0 to 50 vol%), we replaced some of these boulders with matrix material when we built our target asteroid (Extended Data Fig. 2). We explicitly modelled only boulders larger than 2.5 m in diameter, and the space between boulders was filled with matrix material. Boulders smaller than 2.5 m were removed from the SFD because they were too small to be resolved individually. Thus, components smaller than 2.5 m were considered part of the matrix, which was modelled as a granular material with low but limited cohesion. This approach created an asteroid whose interior structure is like that of its surface and whose structure overall is consistent with a gravitational collapse. For the purpose of this study, other deep interior structures were not considered.

The bulk porosity of Dimorphos results from macroporosity between individual rocks and boulders as well as microporosity within rocks. An analysis of reflectance spectra of Didymos indicates that the best meteorite analogues for boulders on Dimorphos are L/LL ordinary chondrites[20–22], which have grain densities of ~3,200–3,600 kg m^{-3} and low microporosities of ~8–10% (ref. [23]). Using the method described by ref. [24] ('Macroporosity calculations for Dimorphos' in Methods), we calculated macroporosities of 38 ± 3% from the boulder SFD in the last complete image taken by DART (ref. [1]) and 34 ± 4% from the global SFDs

Table 1 | Table of fixed and varied target parameters

Fixed parameters	
Target dimensions[1]	177×174×116 m
Target volume[1]	0.00181 km^3
Boulder SFD[19]	See Methods
Boulders at impact location[1]	See Methods
Boulder tensile strength	10 MPa
Boulder porosity	10%
Varied parameters	
Boulder packing	0–50 vol%
Grain density, ρ_g	3,200 or 3,500 kg m^{-3}
Matrix porosity, ϕ_0	35–65%
Matrix cohesion, Y_0	0–500 Pa
Matrix internal friction coefficient, f	0.4–0.7

measured on Dimorphos[19] (Extended Data Fig. 3). The derived macroporosity was primarily determined by the boulder SFD (Extended Data Fig. 4) and the sphericity/roundness of the boulders (Extended Data Fig. 5). Importantly, the macroporosity estimation is largely independent of the assumed minimum boulder size. In our simulations, the initial micropososity within boulders was fixed at 10% and the initial porosity of the matrix (macroporosity + microporosity) was varied between 35% and 65% (Extended Data Fig. 6). Both the porosity in the boulders and in the matrix were modelled using the P-α porosity compaction model[14] with parameters as summarized in Extended Data Table 2.

Based on laboratory measurements of meteorite falls, the average tensile strength of ordinary chondrites is 24 ± 11 MPa, and there is no statistical difference between L and LL types[23]. In all our simulations, the initial material properties of the boulders were kept the same and we employed the tensile strength and fracture model as described in refs. [14,15], with parameters corresponding to a tensile strength $Y_T \approx 20$ MPa for a ~2 cm specimen. For the boulders on Dimorphos, the average $Y_T \approx 10$ MPa (Table 1). However, based on previous impact studies (for example, ref. [18]), we did not expect the impact outcome to be very sensitive to the boulder tensile strength.

The response of the target matrix material to shear deformation is described by a simple pressure-dependent strength model[25,26]. The ability of a material to resist different types of stresses is an indicator of its strength. Granular materials, for instance, may exhibit considerable shear strength due to the presence of van der Waals forces and the particles' inability to separate or slide over each other due to interlocking mechanisms[27–29]. Here we focus on the influence of the shear strength at zero pressure, commonly known as cohesion (or cohesive strength). Another important term in the strength model is the coefficient of internal friction. Although this parameter cannot be directly determined, it is possible to relate it to the angle of repose (Methods) and bound the range of plausible values by making reasonable assumptions. The angle of repose of low-cohesion materials has been measured to be $\theta = 22°$ ($f = 0.4$) for glass beads[30], $\theta = 30°$ ($f = 0.55$) for quartz sand[31] and $\theta = 35–45°$ ($f = 0.7–0.9$) for lunar regolith[32].

On Dimorphos, for a cohesion lower than $Y_0 \approx 4$ Pa, the impact occurs in the gravity-dominated regime in which crater growth is halted by the asteroid's small gravity rather than its cohesion[33]. Therefore, we first model impacts into cohesionless rubble piles (with $Y_0 = 0$ Pa but with a coefficient of internal friction of $f = 0.55$ (ref. [31]), which is equivalent to $\theta \approx 30°$). Given our other assumptions regarding material properties, we consider that these models of impacts into targets with no cohesion provide an upper limit on the possible momentum enhancement that can be achieved from the DART impact for a given asteroid mass.
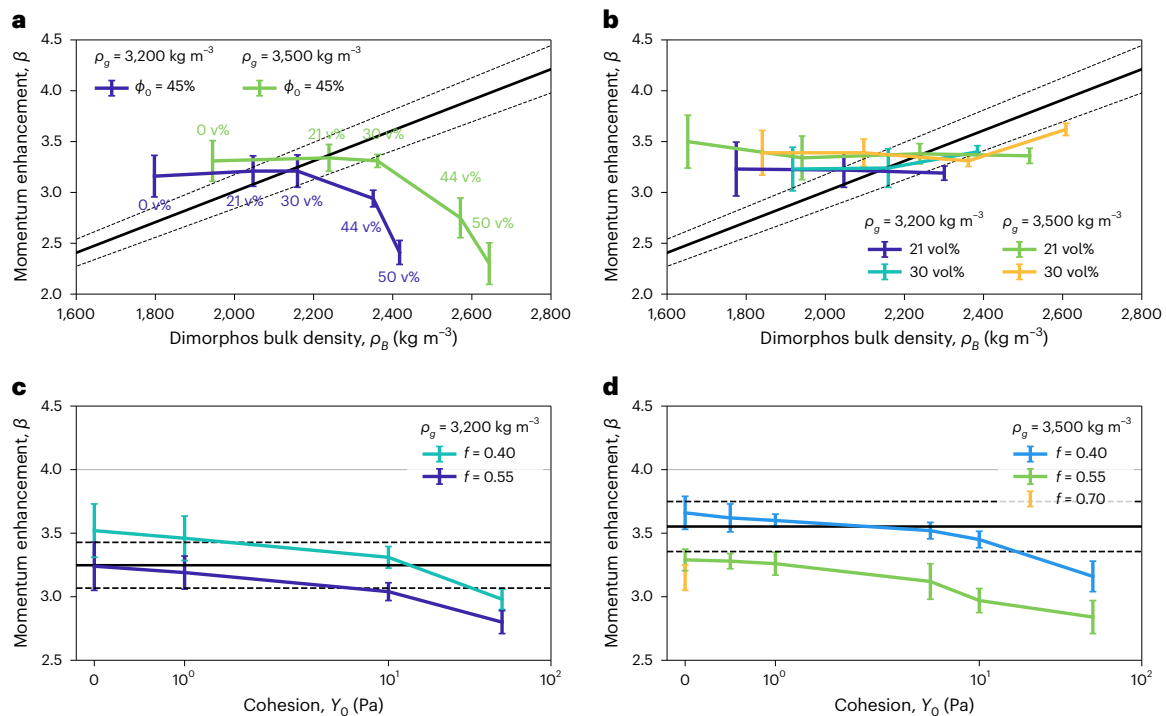
Fig. 1 | Momentum enhancement β as derived from SPH simulations.
a–**d**, Continuous black lines show the β dependence on Dimorphos's bulk density ρ_B derived from dynamical simulations[7] (1σ uncertainty is shown by the dashed lines). Data points that cross a solid black line are consistent with the measured β from the DART impact. The uncertainty for each simulated data point (vertical bars) was calculated from the absolute difference in β calculated from two different methods ('Momentum-enhancement calculations' in Methods). **a**, β as a function of ρ_B for cohesionless targets with the same dimensions as Dimorphos[1] and with boulder volume fractions ranging from 0 vol% (no boulders larger than 2.5 m) to 50 vol%. For fixed target volume (0.00181 km³) and fixed matrix porosity ($\phi_0 = 45\%$), the mass and bulk density of Dimorphos vary with the boulder packing. **b**, β as a function of ρ_B for cohesionless targets with the

matrix porosity varying between 35% and 65% and two boulder packings: 21 and 30 vol%. ρ_B was calculated for a fixed asteroid volume and varies with matrix porosity and boulder packing. **c**, β as a function of matrix cohesion (Y_0) for the DART impact into targets with varying coefficient of internal friction ($f = 0.40$ or 0.55), an assumed grain density $\rho_g = 3,200$ kg m⁻³ and 30 vol% boulder packing. The horizontal line shows β derived from dynamical simulations for a target with $\rho_B = 2,160$ kg m⁻³ (minimum density consistent with the results in **a** and **b**). **d**, β as a function of Y_0 for the DART impact into targets with $f = 0.40$–0.70, $\rho_g = 3,500$ kg m⁻³ and 30 vol% boulder packing. The horizontal line shows β derived from dynamical simulations for a target with $\rho_B = 2,360$ kg m⁻³ (maximum density consistent with the results in **a** and **b**).

The momentum enhancement β was calculated using two distinct methods. For the first method, β was calculated by summing the momentum over all the SPH particles with ejection velocities larger than the escape velocity v_{esc}. For a given impact, the magnitude of ejecta momentum in the direction of the net ejecta momentum is given by

$$p_{ej} = \left| \sum m_e \mathbf{v}_{ej} \right|, \tag{1}$$

where m_e and $\mathbf{v}_{ej}$ are the mass and velocity vector of individual SPH particles, respectively. The p_{ej} calculation takes the gravitational influence of Dimorphos into account. However, it does not account for the gravitational influence of Didymos. The second method, described in ref. 34, tracks the velocity magnitude of the asteroid centre of mass postimpact by summing the momentum of all material that remained below the escape velocity after the reaccumulation of the ejecta. The absolute difference in β resulting from the two calculation methods was used to calculate the error of our reported β values.

Results

First, we varied the boulder volume fraction (the volume fraction of objects >2.5 m in size) within the target between 0 and 50 vol%, while keeping the asteroid volume constant (Table 1). As a result, the mass and the bulk density of the asteroid varied with the boulder packing. Our simulations show that β is relatively insensitive to the boulder volume fractions up to ~30 vol% (Fig. 1a). For boulder volume fractions larger than about 30 vol%, the number of boulders much larger than

the projectile close to the impact point is high enough that the crater efficiency and, subsequently, β are drastically reduced by boulder interlocking[35] and possibly armouring[36], which hinder crater growth. These results indicate that at least the surface and shallow subsurface of Dimorphos have a low volume fraction of boulders larger than 2.5 m (less than ~40 vol%), which is consistent with the last few images sent by DART before impact[1].

Our simulation results for the DART impact on a cohesionless surface of Dimorphos also provide a means to constrain the bulk density of the asteroid using the measured β (Fig. 1b), assuming a grain density in the range 3,200–3,500 kg m⁻³. For a body with a fixed volume and grain density (Table 1), the bulk density is influenced by its porosity. The dominant effect of additional target porosity is a reduction in the bulk density of the target rather than a reduction in ejecta from compaction of the pore space. For example, decreasing the bulk density of Dimorphos will increase the overall crater size and decrease the asteroid's mass (for a fixed volume) and escape velocity. This allows a greater total volume of ejecta to escape, but the ejecta mass is similar. Increasing the bulk density has the opposite effect. The consequence is that the total momentum of escaping ejecta measured constrains the target bulk density and porosity: for a cohesionless surface of Dimorphos, the upper bound on β (~3.6) implies that the bulk density of Dimorphos is less than the current best estimate of the asteroid's bulk density of 2,400 kg m⁻³ (ref. 1). Thus, Dimorphos is probably more porous and, therefore, may have a rubble-pile structure throughout the whole body.
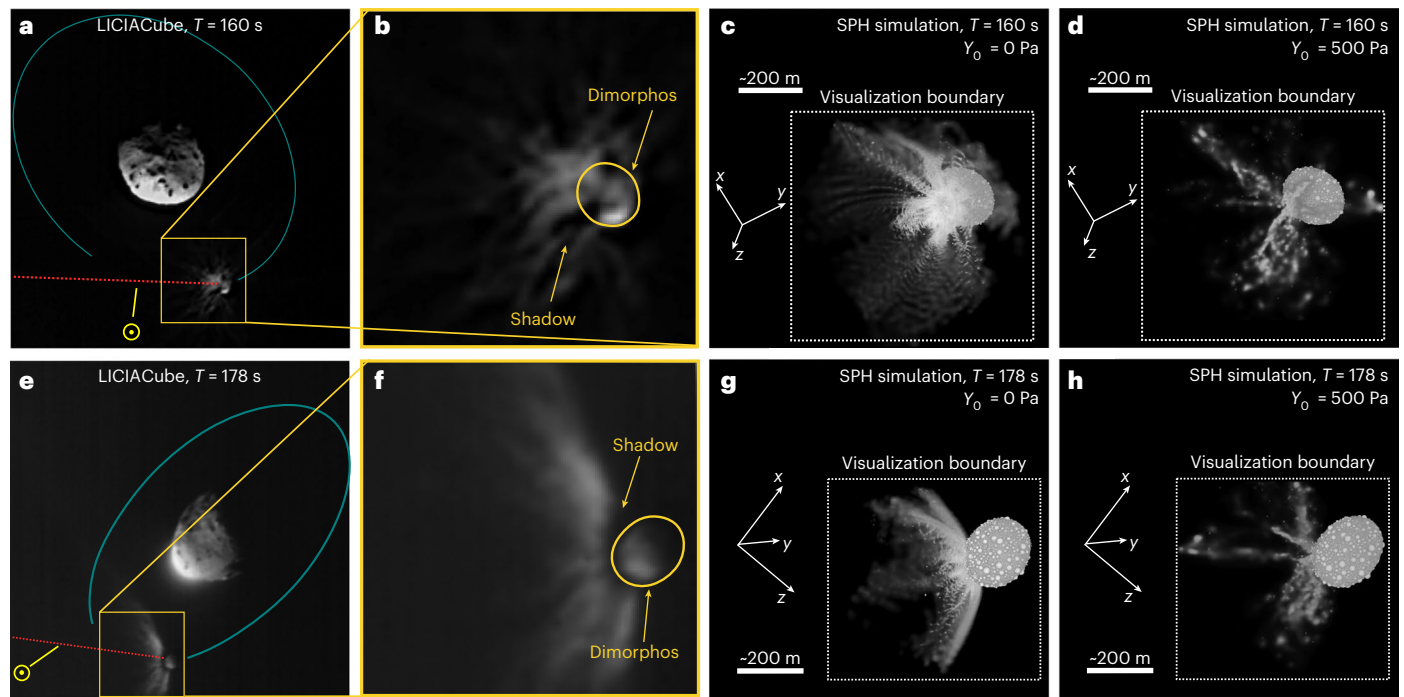
Fig. 2 | LICIACube images of the expanding ejecta cone compared with SPH simulation results. a, Image acquired by the LUKE instrument onboard LICIACube at a distance of ~76 km, 160 s after the impact. **b**, Zoomed-in image of Dimorphos and impact ejecta. The approximate outline of the asteroid is shown in yellow. The ejecta curtain exhibits undulations, filamentary patterns and shadows. **c**, Bern SPH simulation of the DART impact into a cohesionless, rubble-pile Dimorphos-sized target (with $f = 0.55$ and $\phi_0 = 45\%$) at $T = 160$ s.

Due to the limited visualization domain, only a portion of the ejecta are shown. **d**, Simulation of the impact into a rubble-pile Dimorphos-sized target with $Y_0 = 500$ Pa ($\beta = 2.26 \pm 0.28$). **e**, Image acquired by LUKE at a distance of ~71 km, 178 s after the impact. **f**, Zoomed-in image of Dimorphos and impact ejecta. **g**, Same as **c** but at $T = 178$ s. **h**, Same as **d** but at $T = 178$ s. The optical depth of the ejecta cone is not computed for this comparison between the observations and simulation output. Panels **a**, **b**, **e**, **f** adapted from ref. 4, Springer Nature Limited.

Since the surface strength of Dimorphos is poorly constrained, for a fixed boulder distribution (30 vol%), matrix porosity ($\phi_0 = 45\%$) and grain density ($\rho_g = 3,200$ or $3,500$ kg m^{-3}), we varied the matrix material cohesion ($Y_0 = 0$–50 Pa) and coefficient of internal friction ($f = 0.4$–0.7) (Table 1 and Methods). Several possible combinations of cohesion, coefficient of internal friction and bulk density could result in the observed deflection and account for the observed momentum enhancement (Fig. 1c,d). Despite this non-uniqueness, it is possible to bound the range of plausible values by making reasonable assumptions since $f = 0.4$ is a lower limit for geological materials. For a target with $f = 0.4$ and $\phi_0 = 45\%$, the cohesion on the surface of Dimorphos is probably lower than ~50 Pa (Fig. 1c,d). However, lower bulk densities ($\rho_B < 2,000$ kg m^{-3}) or higher matrix porosities ($\phi_0 > 55\%$) would require higher cohesion to match the observations (Fig. 1).

Ejecta curtain opening angle and morphology

In our simulations of the DART impact into Dimorphos-like rubble-pile targets, we observed the temporal changes of the ejecta cone opening angle and studied the dependences on target properties. We found no notable dependences of ejecta cone opening angle on the friction coefficient of the targets. This finding contrasts with the strong dependence of the cone opening angle on the coefficient of internal friction that is found in simulations[37] of the DART impact into homogeneous planar targets. Our present simulations of impacts into Dimorphos-like rubble piles found that the ejecta cone opening angle and ejecta mass depend on target cohesion. Figures 2 and 3 compare results for cohesionless targets ($Y_0 = 0$ Pa) with those for cohesive targets ($Y_0 = 500$ Pa).

The ejecta plume for the cohesionless target (Fig. 2c,g) is more massive than that for the cohesive target (Fig. 2d,h). For both cases, the fastest ejecta, released shortly after the impact with velocities higher than a few tens of m s^{-1}, form a cone opening angle $\omega \approx 90°$ (Fig. 3a,b). Such fast ejecta are influenced by the spacecraft geometry (for example, refs. 38,39), which is highly simplified in this study. On the other hand, slower ejecta, released at late times after the impact (hundreds to thousands of seconds) with velocities $v_{esc} < v < 5$ m s^{-1}, form a wider ejecta cone angle of ~140° (at 1 m s^{-1}, Fig. 3a) for the cohesionless target. For the cohesive target ($Y_0 = 500$ Pa), crater growth ceases about 100 s after the impact, before the crater grows large enough for the ejection angle to be influenced by target curvature. In this case, the maximum ejecta opening angle is ~120° (at 1 m s^{-1}, Fig. 3b). On the other hand, for the low-cohesion targets, the mass ejected at low velocities ($v_{esc} < v < 10$ m s^{-1}) greatly exceeds the low-velocity ejecta mass from the cohesive target ($Y_0 = 500$ Pa), implying a larger cratering efficiency and crater growth continuing to later times, resulting in a wider cone opening angle influenced by target curvature.

The characteristics of the ejecta plume observed by LICIACube provide constraints regarding the target cohesion. At time after impact $T = 160$ s, LICIACube's LUKE acquired images show ejecta concentrated into rays, which cast shadows along the ejecta cone (Fig. 2a,b). At $T = 178$ s, the bottom of the ejecta cone and the surface of Dimorphos are obscured by the shadow cast by the ejecta (Fig. 2e,f and Extended Data Fig. 7). The shadow observed at $T = 178$ s implies that crater growth and the release of low-speed ejecta continued to that time, consistent only with low-cohesion target cases, for example, ref. 40.

Images obtained from LICIACube (ref. 4) and Hubble Space Telescope (HST) observations[5] revealed a wide ejecta cone angle, estimated to be $\omega \approx 115°$–$139°$ (Extended Data Table 3). These observations were used to determine the ejecta opening angle at specific times, up to 3 min after the impact for LICIACube (ref. 4) and up to 8 h after the impact for HST[5]. To compare simulations results with observations of
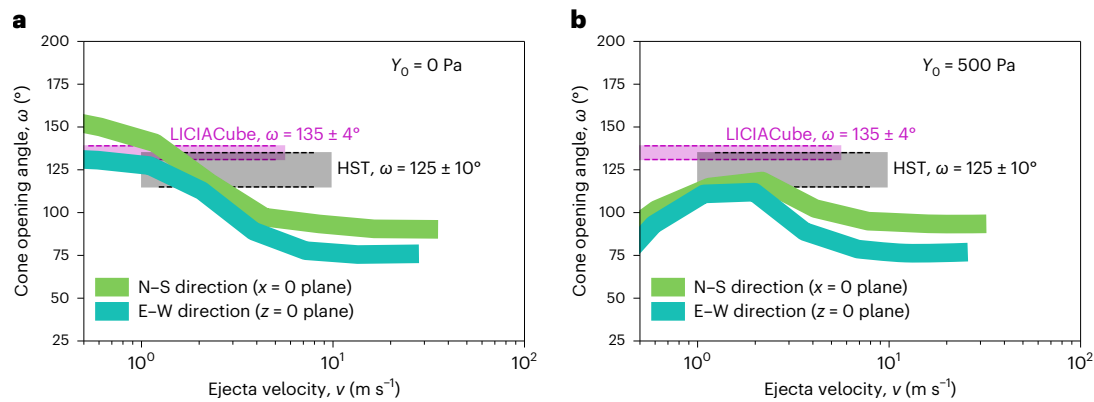
Fig. 3 | Ejecta cone opening angle. a, Cone opening angle derived from cohesionless ($Y_0 = 0$ Pa) SPH simulations (shown in Fig. 2c,g) in the N–S direction ($x = 0$ plane) and in the E–W direction ($z = 0$ plane). **b**, Cone opening angle derived from SPH simulations with $Y_0 = 500$ Pa in the N–S direction ($x = 0$ plane) and in the E–W direction ($z = 0$ plane). The cone opening angle derived from observations is plotted for comparison in both **a** and **b**. $\omega = 135 \pm 4°$ was measured from

LICIACube data based on the opening angle at the base of the cone at $T \approx 170$ s, resulting in ejecta velocities in the range of a few cm s^{-1} to a few tens of m s^{-1} (ref. 4). $\omega = 125 \pm 10°$ was measured from HST data for ejecta in the range 1–10 m s^{-1} (ref. 5). Temporal evolution measurements of the observed ejecta cone were not possible due to the limited observation window.

the ejecta opening angle at a specific time after impact, we determined the implied ejecta velocity at the base of the visible cone in the LICIA-Cube images[4] (Fig. 2e,f) using its distance above the surface and time after impact (Fig. 3).

Overall, we found that to qualitatively reproduce the amount of material observed in the ejecta cone (Fig. 2c,g) as well as the observed cone opening angle of up to $\omega \approx 139°$, Dimorphos's surface cohesion must not exceed ~500 Pa. From our suite of numerical simulations with the assumed boulder packing, matrix porosity and grain density summarized in Table 1, we found that the target case with $f = 0.55$, $\rho_B = 2,200$ kg m^{-3} and Y_0 less than a few pascals is consistent with the target mechanical properties inferred from surface geology[41] and produces a β value (Fig. 1), excavation timescale (Fig. 2) and ejecta opening angle (Fig. 3) most consistent with observations.

Deformation

Observations from the first few hours after impact imply that more than $1.3–2.2 \times 10^7$ kg of ejecta were released from the DART impact (equivalent to 0.3–0.5% of Dimorphos's mass, assuming a bulk density of 2,400 kg m^{-3})[6]. Our simulation results for weak ($Y_0 < 50$ Pa), Dimorphos-like targets ($f = 0.55$ in Fig. 1c) show that the amount of ejected material could be as high as 1% of Dimorphos's mass (Fig. 4a). Moreover, up to 8% of Dimorphos's mass may have been displaced or ejected at below the escape velocity of Dimorphos. In all impact scenarios simulated here, the DART impact does not produce a conventional impact crater but instead causes global deformation of the target (Fig. 4b).

The outcome of the impact in terms of the postimpact target morphology is highly sensitive to the target cohesion. For a cohesionless target, the ratio of the major to intermediate axes a/b could have changed from the reported pre-impact value of 1.02 ± 0.02 (ref. 1) to as much as 1.2. Such a large change in the a/b ratio is detectable with the highest-quality postimpact light curve data[13,42].

A global deformation of Dimorphos would have modified the gravitational field between Didymos and Dimorphos with important implications for its orbit. The shape change would cause an additional perturbation to Dimorphos's orbit, on top of those caused by the spacecraft momentum and ejecta recoil, and this effect can account for a few seconds to several minutes of the observed orbit period change (~33 min), depending on the magnitude of the deformation[43]. Any deformation would alter Dimorphos's mass distribution and affect its postimpact rotation state (for example, refs. 44,45).

Implications for binary asteroid system formation

Our numerical simulations suggest that Dimorphos is probably a rubble-pile asteroid with a bulk density comparable to or lower than that of Didymos. Our calculations based on the observed boulder SFD indicate that the macroporosity estimate for the surface of Dimorphos (~35%) is approximately twice the value obtained for the surface of Ryugu, as determined through the same method[24,46], but is comparable with the macroporosity of Itokawa[24,47]. However, note that this estimate is only a rough approximation due to the limited data currently available. The upcoming Hera mission will be able to provide better constrains.

Our findings serve as crucial evidence regarding the origin of Dimorphos as a secondary in a double asteroid system. To maintain its structural stability given its rapid rotation period of 2.26 h, the primary, Didymos, probably requires a higher cohesive strength, estimated to be of the order of tens of pascals[48]. This level of cohesion can be attributed to van der Waals forces acting between the fine regolith grains[49] or to a coherent inner core[50]. However, our best-fitting scenarios indicate that Dimorphos, the satellite of Didymos, exhibits a cohesive strength of less than a few pascals. This observed disparity in cohesive strength between Didymos and Dimorphos suggests a potential scarcity of fine grains within Dimorphos's structure as well as a weak and fragmented internal structure.

The material properties estimated in our study support the hypothesis that Dimorphos formed through rotationally or impact-induced mass shedding and subsequent reaccumulation from Didymos. The accretion of orbiting mass shed from Didymos occurs over a period of several days to years[51], during which fine grains tend to escape from the system due to solar radiation pressure[52]. As a result, the accreted satellite, Dimorphos, has limited fines and cohesion.

Although the mechanical properties of Dimorphos resemble those of Ryugu and Bennu (for example, refs. 17,53–55), these findings may not be applicable to single, small, S-type asteroids and specifically to their moons. The implications of our study may extend beyond Dimorphos and provide valuable insights into the formation processes of similar small S-type binary asteroid systems.

Moreover, since the DART spacecraft probably caused global deformation of Dimorphos, we can infer that similarly formed asteroid moons are easily reshaped and their surfaces are relatively young[16]. Overall, the findings of this study provide valuable information for understanding the formation and characteristics of binary asteroids and will inform future exploration and asteroid deflection efforts.
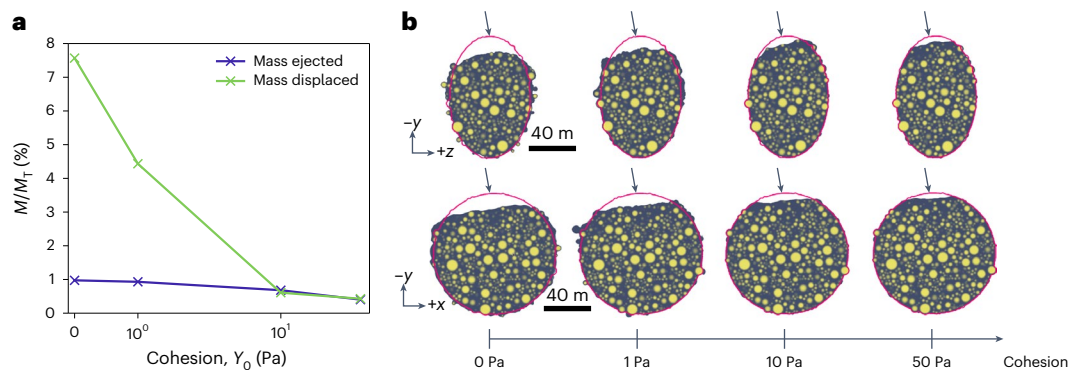
Fig. 4 | Global deformation of Dimorphos. a, Total target mass ejected with speeds above v_{esc} and total target mass displaced or ejected below v_{esc}, normalized by the initial target mass M_T for a Dimorphos-like target with $f = 0.55$, $\phi_0 = 45\%$ and cohesion levels between $Y_0 = 0$ and 50 Pa. **b**, Two-dimensional slices (taken at $x = 0$ in the y–z plane and at $z = 0$ in the x–y plane), at $T \approx 1$ h after the impact. The boulder material is shown in yellow and the matrix material is shown in blue. The red contours show the initial target profile before the impact. The black arrows show the impact direction.

Methods

Macroporosity calculations for Dimorphos

The bulk porosity of Dimorphos results from macroporosity between individual rocks and microporosity within rocks. The macroporosity of a granular assembly is affected by the particle SFD, interparticle friction and the packing history[56]. Numerical simulations of gravitational aggregation[29,50,56], which is one of the probable formation mechanisms for Dimorphos-like secondaries[51], can be used to estimate the initial packing of the boulders within the asteroid.

We use the method described by ref. 24 to calculate the surface macroporosity from the SFD of boulders at the impact location[1] and the global boulder SFD on the illuminated side of Dimorphos[19] (Extended Data Fig. 4a). We used a cumulative Weibull (Rosin–Rammler) distribution[24,57,58] to represent the two SFDs:

$$N(D) = N_T \exp(-3(D/\lambda)^\beta)/\beta, \qquad (2)$$

where D is the boulder size and N_T, λ and β are constants (Extended Data Fig. 4a). We found that the fitting constants N_T, λ and β vary with the assumed minimum boulder diameter D_{min}, as seen in Extended Data Fig. 4b,c,d.

We used Monte Carlo code to generate a Gaussian distribution for the particle bulk density (including the approximate microporosity), the initial boulder packing, the boulder sphericity and the boulder roundness. For the bulk density calculations, we assumed a grain density of $3{,}500 \pm 100$ kg m^{-3}, with microporosity ~10% (ref. 23), giving a mean value of $3{,}220$ kg m^{-3} (Extended Data Fig. 5a). Based on the pkdgrav simulations described in 'Numerical model', we considered an initial packing with a mean value of 39% (Extended Data Fig. 5b). Preliminary estimates of the sphericity and the roundness of boulders were derived from the last complete image taken by the DRACO camera onboard DART[59], giving mean values of 0.74 and 0.56, respectively (Extended data Fig. 5c,d). Other observational output constraints are given in Extended Data Table 3.

Numerical model

In this work, we used the Bern SPH shock physics code[14,15,60]. The code was originally developed by refs. 60,61 to model the collisional fragmentation of rocky bodies. It was later parallelized[62] and further extended by refs. 14,15 to model porous and granular materials. The most recent version of the code includes a tensile fracture model[60], a porosity model based on the P-α model[14], pressure-dependent strength models[15] and self-gravity. The Bern SPH code has been validated in a number of studies (for example, refs. 63,15) and benchmarks against other codes (for example, ref. 64).

We modelled the DART impact and DART-like impacts into rubble-pile ellipsoidal targets composed of different distributions of spherical boulders embedded into a matrix material (Extended Data Fig. 7). We tracked the evolution of the ejecta and of the target for up to 1 h after the impact. Due to the relatively short timescales modelled, the rotation of Dimorphos around Didymos and Didymos's gravity were not accounted for. To obtain realistic configurations of boulders, we used the rubble-pile model with Dimorphos's surface boulder SFD, which was generated from the gravitational accumulation simulations using the N-body code pkdgrav (ref. 65).

Projectile. The DART spacecraft bus was approximately $1.2 \times 1.3 \times 1.3$ m in size, with structures extending to approximately $1.8 \times 1.9 \times 2.6$ m (ref. 1). Additionally, the spacecraft featured two large solar arrays, each measuring 8.5 m in length. The spacecraft weighed 579.4 ± 0.7 kg at impact[1]. Studies of the influence of the spacecraft geometry on cratering[39] show that a simple solid representation underestimates the surface area of the impact compared to a ~20 m complex projectile. Moreover, the penetration depth of a solid sphere is larger than for the spacecraft itself. However, ref. 38 showed that the projectile geometry affects only the very early, fast ejecta generated from within the coupling zone. Therefore, due to resolution constraints, here we simplify the projectile geometry. To match the penetration depth of the spacecraft bus, we modelled the projectile as an under-dense aluminium sphere, as opposed to a solid sphere (radius $r \approx 0.52$ m and bulk density $\delta = 1{,}000$ kg m^{-3}) with the equivalent mass of the DART spacecraft. For the large cratering efficiencies studied here, for which the crater cavity grows many times larger than the DART spacecraft, we considered that a spherical projectile is a reasonable approximation for a DART-like impact.

Material model. We modelled both the boulders and the matrix material using the Tillotson equation of state for basalt[61,66], with modified initial grain densities of $\rho_g = 3{,}200$ and $3{,}500$ kg m^{-3}.

For the response of the matrix material to shear deformation, we applied a simple pressure-dependent strength model, typical of geological materials[25,26], with asymptotes to a certain shear strength at high pressures. The Lundborg strength model describes the yield strength as:

$$Y = Y_0 + \frac{fP}{1 + fP/(Y_{dm} - Y_0)}, \qquad (3)$$

where P is pressure, f is the coefficient of internal friction and Y_{dm} is the limiting strength at high pressure. For the weak asteroid

materials considered in this study, we used a constant cohesion Y_0 with a strain-based weakening model that prevents artificial clumping (like the approach used in ref. 67). Our model uses a linear relation between cohesion Y_0 and total strain ϵ_{tot}, and it is assumed that for $\epsilon_{tot} \geq 1$, cohesion is lost. When modelling the matrix material, the tensile strength was defined by extrapolating the yield strength (versus pressure) curve (equation (3)) to intersect the pressure axis. Additionally, we limited the maximum negative pressure to $P_{min} \geq -Y_0$. To compute the coefficient of internal friction f from the measured angle of response ϕ (refs. 32,68), we followed the relation described in ref. 64:

$$f = \frac{2\sqrt{2}\sin(\phi)}{3 - \sin(\phi)}. \tag{4}$$

We varied the cohesion Y_0 between 0 and 50 Pa and the coefficient of internal friction f between 0.4 and 0.7.

Tensile strength of boulders. Based on laboratory measurements of meteorite falls, the average tensile strength of ordinary chondrites[69] is 24 ± 11 MPa, with no statistical difference between the L and LL types[23]. However, measurements of individual specimens span from a few megapascals up to ~100 MPa. In all our simulations, the initial material properties of the boulders were kept the same and we employed the tensile strength and fracture model as described in refs. 14,15, with parameters corresponding to a tensile strength $Y_T \approx 20$ MPa for a ~2 cm specimen. For the boulders on Dimorphos, the average $Y_T \approx 10$ MPa.

Porosity model. The initial porosity of the boulders was fixed at 10% (refs. 70,71), whereas the porosity of the matrix (which includes boulders smaller than 2.5 m) was varied between 35% (25% macroporosity + 10% microporosity) and 65% (55% macroporosity + 10% microporosity). Both were modelled using the P versus α porosity compaction model[72,73]. The full description of the P versus α model implemented in the Bern SPH code is given by ref. 14. Here we used a simplified version of the P versus α model with a single power-law slope defined by the solid pressure P_s, elastic pressure P_e, exponent n, initial distension α_0 and distension at the transition from the elastic regime α_e:

$$\alpha(P) = \begin{cases} 1, & \text{if } P_s < P. \\ (\alpha_e - 1)\left(\frac{P_s - P}{P_s - P_e}\right)^n + 1, & \text{otherwise.} \end{cases} \tag{5}$$

We assumed that $\alpha_e = \alpha_0$. The input parameters from the matrix and for the boulders are summarized in Extended Data Table 2. Without crush-curve measurements of the surface material, our input parameters were informed by experimental quasi-static crush curves of Earth analogues and lunar regolith. We defined crush curves that have crushing strengths higher than the crushing strengths for sand[74,75] but lower than the crushing strength for lunar regolith[76,77]. Extended Data Fig. 6 compares our P versus α crush curves with the experimental quasi-static crush curves for lunar dust[76], gypsum (50% porosity)[78], Lane Mountain No. 70 sand (44% porosity)[75] and Ottawa sand (30–45% porosity)[74].

Modelling approach for the late-stage evolution. Due to the vastly different timescales of the shock-wave propagation and crater formation, it is difficult to numerically model the entire crater formation on small, weak asteroids (~100–1,000 m). To ensure numerical stability, the maximum time step in a shock physics code is limited by the Courant criterion. In SPH, the Courant criterion requires that the time step dt is smaller than the simulation resolution divided by the speed of sound in the target, c_s. To model DART-like impacts on Dimorphos, the maximum time step must therefore be $\Delta t < \text{resolution}/c_s \approx 10^{-4}$ s. On the other hand, the crater formation and ejecta reaccumulation time in the gravity regime can last up to a few hours. Here we applied a transition to a low-speed medium in the shock physics code calculation.

At a time $t_{transition}$ after the initial shock has passed, movement of the target material is governed only by low velocities, $v_{material} \ll c_s$, and we can switch to a low-speed medium (using a fast time integration scheme). In this step, we applied a simplified Tillotson equation of state in which all energy-related terms are set to zero. The remaining leading term of the equation of state is governed by the bulk modulus $P = A(\rho/\rho_0 - 1)$, which also determines the magnitude of the sound speed. At $t_{transition} = 0.5$, 20 and 500 s, we used $A = 359$ MPa, 3.59 MPa and 35.9 kPa, respectively. The shear modulus was also reduced proportionally. The Bern SPH fast-integration scheme has been validated against laboratory experiments[18] and was recently successfully applied in modelling the impact of the Hayabusa2 Small Carry-on Impactor[17].

Rubble-pile model of Dimorphos
To obtain realistic configurations of boulders, we used the rubble-pile model with Dimorphos's surface boulder SFD, which was generated from the gravitational accumulation simulations using the N-body code pkdgrav[65]. Extra particles near the surface were removed to more faithfully represent the target topography reported by ref. 1. To explore a large possible range of boulder mass fractions, we removed some of these boulders from the pkdgrav output when we built our SPH models. We defined four different boulder distributions, with ~21, 30, 44 and 50% of the target volume occupied by boulders (Extended Data Fig. 2c). Boulders smaller than $R_{min} = 1.25$ m (2.5 m in diameter) were removed from the SFD due to being too small to be resolved individually. We assumed that they were part of the matrix material that was used to fill the voids between the larger boulders.

Impact site and impact angle. DART impacted Dimorphos at $8.84 \pm 0.45°$ S, $264.30 \pm 0.47°$ E, and the impact angle was $17 \pm 7°$ from the surface normal[1]. The impact was on a boulder-covered terrain, which was mapped using the global digital terrain model from ref. 1 (Extended Data Fig. 1). Using Delaunay triangulation, convex hulls were created for the three largest boulders at the site: a 6.5 m boulder (Atabaque Saxum), a 6.1 m boulder (Bodhran Saxum) and a smaller, 4 m boulder (Caccavella Saxum). These boulders were incorporated into all SPH simulations. The solar arrays made contact with Dimorphos's surface before the spacecraft bus; however, the majority of the impact energy was transferred through the bus, which made up most of the spacecraft's mass at the time of impact[1].

Momentum-enhancement calculations
In a high-velocity impact event, the change in momentum of the asteroid $\Delta \mathbf{P}$ is amplified by the momentum of impact ejecta that escapes the gravitational attraction of the target body[10]. The DART impact changed the orbital period around Dimorphos by ~33 min and was directly measured from ground-based observations[2]. This change in orbital period corresponds to a change in the orbital velocity of about 2.7 mm s^{-1}.

The momentum transferred to the target body relative to the incident momentum of the spacecraft, quantified by the momentum-enhancement factor β, is defined by[7]:

$$M\Delta\mathbf{v} = m\mathbf{U} + m(\beta - 1)(\hat{E}U)\hat{E}, \tag{6}$$

where M is the mass of Dimorphos, $\Delta\mathbf{v}$ is the change in Dimorphos's orbital velocity due to the impact, m is the mass of the DART spacecraft, $\mathbf{U}$ is DART's velocity relative to Dimorphos's at impact and $\hat{E}$ is the net ejecta momentum direction.

The full equation needed to determine the momentum-enhancement factor β from observations is derived in ref. 9 and further discussed in ref. 7. We define β as the total momentum change of the asteroid ΔP divided by the magnitude of the impactor momentum mU:

$$\beta = \Delta P/(mU) = 1 + \frac{p_{ej}}{mU}, \tag{7}$$

where p_{ej} is the magnitude of the vector sum of the momentum of the ejecta.

The value of β depends on both the target material properties and the impact conditions (for example, refs. 11,16,34,38,79,80). A value of $\beta \approx 1$ implies that the impact ejecta made a negligible contribution to the total momentum change, whereas $\beta > 2$ means that the momentum contribution from the impact ejecta was larger than the momentum imparted by the impactor directly.

To affirm the validity of our simulation results, we calculated β using two distinct methods. For the first method, β was calculated by summing over all the SPH particles with ejection velocities larger than the escape velocity v_{esc}. v_{esc} was calculated by summing over all the SPH particles in the simulation. However, we did not consider the gravitational influence of Didymos.

For a given impact, the ejecta momentum is given by

$$p_{ej} = \left| \sum m_e \mathbf{v}_{ej} \right|, \tag{8}$$

where m_e and $\mathbf{v}_{ej}$ are the mass and velocity vector of individual SPH particles, respectively. Note that in some of the tests and analysis presented in the Methods, β is computed with respect to the along-track direction (y) for simplicity. In the impact simulations presented here, we were able to track the impact ejecta, and we performed the β calculation after long periods (up to 1 h after the impact). Therefore, the p_{ej} calculation takes the gravitational influence of Dimorphos into account.

The second method, described in ref. 34, tracks the velocity of the asteroid centre of mass postimpact by summing the momentum of all material that remained below the escape velocity after the reaccumulation of the ejecta. The absolute difference in β resulting from the two calculation methods was used to calculate the error of our reported β value for each simulation.

Resolution tests
So that we could model numerically the very long timescales required to see the impact effects, most of the SPH simulations presented here had a limited spatial resolution of 5.6×10^6 SPH particles. Due to the low resolution employed here, the very fast ($v/U > 10^{-1}$) ejecta was under-resolved, which may cause an overestimation or underestimation of the total ejected mass and ejecta momentum at high speeds.

We performed resolution tests with impacts into a cohesionless target with 30 vol% boulders, $f = 0.55$ and $\phi_0 = 45\%$ using two resolutions: 5.6×10^6 SPH particles and 14.5×10^6 SPH particles. The low-resolution runs overestimated the amount of mass ejected at high velocities, $M(v/U > 10^{-2})$, by a few percent (Supplementary Fig. 1a). In addition, the cumulative ejecta momentum at speeds lower than $v/U < 1e3$ was overestimated by about 6% in the low-resolution run (Supplementary Fig. 1b).

To further study the effects of resolution, we also computed the data from impacts into cohesionless targets with 30 vol% boulders, $f = 0.55$ and $\phi_0 = 45\%$ but where only ~15% of the target (in the y direction) was modelled. These targets with a reduced domain were modelled with 5×10^6 SPH particles and 10×10^6 SPH particles (Supplementary Fig. 2). We see no clear difference compared to Supplementary Fig. 1.

Parameter studies
Target curvature and impact location. For a fixed homogeneous, ellipsoidal target (Extended data Fig. 2, with $\rho_g = 3,500$ kg m^{-3}, $Y_0 = 0$, $f = 0.55$ and $\phi_0 = 45\%$), we considered DART-like impacts at different locations. Location 1 is at $x = 0$ m and $y = 0$ m in the middle of the a and b axes of the asteroid. The impact was vertical. Location 2 is at $x = 0$ m and $z = 0$ m in the middle of the a and c axes. The impact was vertical. Location 3 is the DART impact location at $x = -8.31$ m and $z = -12.69$ m

(ref. 1). Location 4 is the DART impact location with the three boulders at the impact site (Extended Data Fig. 1). Both locations 3 and 4 used the DART spacecraft velocity vector as described in ref. 1 (the impact was modestly oblique).

Supplementary Fig. 3a shows the mass–velocity distribution of the ejecta from impacts at locations 1–4. Supplementary Fig. 3b shows the cumulative ejected momentum as a function of normalized vertical ejection velocity (in the $+z$ direction for location 1 and in the $-y$ direction for locations 2–4). For this target scenario, a vertical DART-like impact at location 1 produced $\beta_z \approx 3.82$ and the impact at location 2 produced $\beta_y \approx 3.74$. At location 3, $\beta_y \approx 3.14$, which means that the impact location and the impact angle reduced $p_{ej(y)}$ by about 18%. At location 4, which has the same geometry as location 3 but has the three boulders at the impact site, $\beta_y \approx 3.06$. These results suggest that the three boulders at the impact location had a minimal effect on β, at least for our assumed impactor shape.

Boulder packing. For a fixed target shape (Extended Data Fig. 2) and material properties ($\rho_g = 3,500$ kg m^{-3}, $Y_0 = 0$ Pa, $f = 0.55$ and $\phi_0 = 45\%$), we investigated the effects of the volume fraction of boulders larger than 2.5 m within the target on the ejecta mass–velocity distribution (Supplementary Fig. 4a) and the momentum–velocity distribution (Supplementary Fig. 4b). The boulders were modelled as spheres. We simulated the DART impact into targets with five different boulder volume fractions: 0, 21, 30, 44 and 50 vol%. All runs included the three boulders at the impact site, including the target with 0 vol% boulders. We found that the DART impact into targets with a boulder packing of 21 and 30 vol% have almost the same ejected mass and ejecta momentum compared to a homogeneous, matrix-only target scenario (within 10%). Moreover, impacts into targets with a boulder packing higher than ~44% show a clear reduction in the ejecta mass and ejecta momentum. For a target with boulder packing of 50 vol%, the cumulative ejecta momentum was reduced by about 40% compared to a similar impact into a homogeneous, matrix-only target. We attribute this reduction in ejecta to a lower cratering efficiency caused by boulder armouring[36] and interlocking[35]. However, the DART impact excavated material only from the upper approximately 15 m, and our models cannot rule out the possibility that the interior of Dimorphos may be more densely packed.

For the same impact scenario, we varied the arrangement of the boulders while keeping the volume boulder packing constant at 44 and 50 vol%. The SFD distribution and the boulders at the impact site were the same. Our results show that the random nature of the boulder distribution causes a variation in the cumulative ejecta momentum of up to 10% (Supplementary Fig. 5).

Grain density. Supplementary Fig. 6 shows the momentum–velocity distributions from the DART impact into Dimorphos-like targets with two grain densities, $\rho_g = 3.2$ and 3.5 kg m^{-3}, for targets with no boulders (0 vol%, Supplementary Fig. 6a) and targets with 30 vol% boulder packing (Supplementary Fig. 6b). For the DART impact scenario, the grain density influences only the low-velocity ejecta ($v/U < 10^{-4}$).

Cohesion and coefficient of internal friction. The normalized ejected mass at speeds greater than v as a function of the normalized ejection speed v/U is shown for the DART impact into targets with varying cohesion (between 0 and 50 Pa; Supplementary Fig. 7a) and for targets with a varying coefficient of internal friction (between 0.40 and 0.70; Supplementary Fig. 8a). Supplementary Figs. 7b and 8b show the cumulative ejected momentum as a function of ejection speed.

For the range of target cohesions investigated here, only the ejecta slower than ~1 m s^{-1} was affected, which means that the effects are seen in terms of β and the amount of target deformation but not in terms of the morphology of ejecta at the time of the LICIACube observations (Fig. 2).

Ejecta mass and cone orientation

Supplementary Fig. 9 shows the mass of ejecta that escapes Dimorphos ($v > v_{esc}$) and contributes towards the β calculation (Fig. 1).

Based on the analysis of the HST images taken within $T + 8.5$ h, which show ejecta structures moving away from Didymos at speeds greater than 1 m s^{-1}, the ejecta cone centre is directed towards (right ascension (RA), declination (dec.)) = $(141 \pm 8°, 25 \pm 6°)$ or $(120 \pm 9°, 10 \pm 7°)$[5]. The direction of the ejecta cone with projected velocities between a few and ~500 m s^{-1} from LICIACube images[4] is (RA, dec.) = $(137 \pm 9°, 19 \pm 12°)$. An analysis of both HST and LICIACube data gives the direction of the ejecta cone as (RA, dec.) = $(138°, +13°)$ with an uncertainty of 15° (ref. 7). Our analysis reveals that at $T = 160$ s, the direction of the ejecta momentum vector is consistent with the observed cone direction within 1σ uncertainty (Fig. 3a and Supplementary Fig. 10), which suggests that our simulation provides a reasonable estimate of the direction of the plume. However, our analysis of all ejecta, with speeds ranging from the escape velocity ($v \approx v_{esc}$) to km s^{-1}, as analysed at the end of the ejecta production ($T \approx 2,000$ s), predicts a slightly different direction of (RA, dec.) = $(150.5 \pm 4°, 12 \pm 5°)$ (Supplementary Fig. 10). This indicates that the direction of the observed segment of the ejecta plume may not necessarily reflect the true direction of the momentum-enhancement vector, as computed from the entire plume[7], but may be subject to a bias based on the velocity range at which it is observed.

Data availability

Additional supporting information and input data for the model simulations used in this work are archived on Zenodo (https://doi.org/10.5281/zenodo.10246671).

Code availability

A compiled version of the Bern SPH code as well as the necessary input files are available from the corresponding author upon request. The SPH data visualization was produced using the National Center for Atmospheric Research software Visualization and Analysis Platform for Ocean, Atmosphere, and Solar Researchers (VAPOR v.3.8.0) (https://doi.org/10.5281/zenodo.7779648).

References

1. Daly, R. T. et al. Successful kinetic impact into an asteroid for planetary defence. *Nature* **616**, 443–447 (2023).
2. Thomas, C. A. et al. Orbital period change of Dimorphos due to the DART kinetic impact. *Nature* **616**, 448–451 (2023).
3. Dotto, E. et al. LICIACube – the light Italian cubesat for imaging of asteroids in support of the NASA DART mission towards asteroid (65803) Didymos. *Planet. Space Sci* **199**, 105185 (2021).
4. Dotto, E. et al. The Dimorphos ejecta plume properties revealed by LICIACube. *Nature* (2023).
5. Li, J.-Y. et al. Ejecta from the DART-produced active asteroid Dimorphos. *Nature* **616**, 452–456 (2023).
6. Graykowski, A. et al. Light curves and colors of the ejecta from Dimorphos after the DART impact. *Nature* **616**, 461–464 (2023).
7. Cheng, A. F. et al. Momentum transfer from the DART mission kinetic impact on asteroid Dimorphos. *Nature* **616**, 457–460 (2023).
8. Michel, P. et al. The ESA Hera mission: detailed characterization of the DART impact outcome and of the binary asteroid (65803) Didymos. *Planet. Sci. J.* **3**, 160 (2022).
9. Rivkin, A. S. et al. The Double Asteroid Redirection Test (DART): planetary defense investigations and requirements. *Planet. Sci. J.* **2**, 173 (2021).
10. Holsapple, K. A. & Housen, K. R. Momentum transfer in asteroid impacts. I. Theory and scaling. *Icarus* **221**, 875–887 (2012).
11. Raducan, S. D., Davison, T. M., Luther, R. & Collins, G. S. The role of asteroid strength, porosity and internal friction in impact momentum transfer. *Icarus* **329**, 282–295 (2019).
12. Stickle, A. M. et al. Effects of impact and target parameters on the results of a kinetic impactor: predictions for the Double Asteroid Redirection Test (DART) mission. *Planet. Sci. J.* **3**, 248 (2022).
13. Pravec, P. et al. Photometric observations of the binary near-Earth asteroid (65803) Didymos in 2015–2021 prior to DART impact. *Planet. Sci. J.* **3**, 175 (2022).
14. Jutzi, M., Benz, W. & Michel, P. Numerical simulations of impacts involving porous bodies: I. Implementing sub-resolution porosity in a 3D SPH hydrocode. *Icarus* **198**, 242–255 (2008).
15. Jutzi, M. SPH calculations of asteroid disruptions: the role of pressure dependent failure models. *Planet. Space Sci* **107**, 3–9 (2015).
16. Raducan, S. D. & Jutzi, M. Global-scale reshaping and resurfacing of asteroids by small-scale impacts, with applications to the DART and Hera missions. *Planet. Sci. J.* **3**, 128 (2022).
17. Jutzi, M., Raducan, S. D., Zhang, Y., Michel, P. & Arakawa, M. Constraining surface properties of asteroid (162173) Ryugu from numerical simulations of Hayabusa2 mission impact experiment. *Nat. Commun.* **13**, 7134 (2022).
18. Ormö, J. et al. Boulder exhumation and segregation by impacts on rubble-pile asteroids. *Earth Planet. Sci. Lett.* **594**, 117713 (2022).
19. Pajola, M. et al. The boulder size-frequency distribution derived from DART/DRACO images of Dimorphos: first results. In *Proc. 54th Lunar and Planetary Science Conference* 1314 (LPI, 2023).
20. de León, J., Licandro, J., Duffard, R. & Serra-Ricart, M. Spectral analysis and mineralogical characterization of 11 olivine-pyroxene rich NEAs. *Adv. Space Res.* **37**, 178–183 (2006).
21. Dunn, T. L., Burbine, T. H., Bottke, W. F. & Clark, J. P. Mineralogies and source regions of near-Earth asteroids. *Icarus* **222**, 273–282 (2013).
22. Ieva, S. et al. Spectral rotational characterization of the Didymos system prior to the DART Impact. *Planet. Sci. J.* **3**, 183 (2022).
23. Flynn, G. J., Consolmagno, G. J., Brown, P. & Macke, R. J. Physical properties of the stone meteorites: implications for the properties of their parent bodies. *Geochemistry* **78**, 269–298 (2018).
24. Grott, M. et al. Macroporosity and grain density of rubble pile asteroid (162173) Ryugu. *Geophys. Res. Planets* **125**, e2020JE006519 (2020).
25. Lundborg, N. The strength-size relation of granite. *Int. J. Rock Mech. Min. Sci. Geomech. Abstr.* **4**, 269–272 (1967).
26. Collins, G. S., Melosh, H. J. & Ivanov, B. A. Modeling damage and deformation in impact simulations. *Meteorit. Planet. Sci.* **39**, 217–231 (2004).
27. Sánchez, P. & Scheeres, D. J. The strength of regolith and rubble pile asteroids. *Meteorit. Planet. Sci.* **49**, 788–811 (2014).
28. Scheeres, D. J. et al. The dynamic geophysical environment of (101955) Bennu based on OSIRIS-REx measurements. *Nat. Astron.* **3**, 352–361 (2019).
29. Ferrari, F. & Tanga, P. The role of fragment shapes in the simulations of asteroids as gravitational aggregates. *Icarus* **350**, 113871 (2020).
30. Lajeunesse, E., Monnier, J. B. & Homsy, G. M. Granular slumping on a horizontal surface. *Phys. Fluids* **17**, 103302 (2005).
31. Lube, G., Huppert, H. E., Sparks, R. S. J. & Hallworth, M. A. Axisymmetric collapses of granular columns. *J. Fluid Mech.* **508**, 175–199 (2004).
32. Mitchell, J. K. et al. Mechanical properties of lunar soil: density, porosity, cohesion and angle of internal friction. *Lunar Planet. Sci. Conf. Proc.* **3**, 3235 (1972).
33. Cheng, A. F. et al. Model of double asteroid redirection test impact ejecta plume observations. *Planet. Sci. J.* **3**, 131 (2022).
34. Syal, M. B., Owen, J. M. & Miller, P. L. Deflection by kinetic impact: sensitivity to asteroid properties. *Icarus* **269**, 50–61 (2016).
35. Raducan, S. D., Jutzi, M., Zhang, Y., Ormö, J. & Michel, P. Reshaping and ejection processes on rubble-pile asteroids from impacts. *Astron. Astrophys.* **665**, L10 (2022).

36. Tatsumi, E. & Sugita, S. Cratering efficiency on coarse-grain targets: implications for the dynamical evolution of asteroid 25143 Itokawa. *Icarus* **300**, 227–248 (2018).

37. Raducan, S. D., Davison, T. M. & Collins, G. S. Ejecta distribution and momentum transfer from oblique impacts on asteroid surfaces. *Icarus* **374**, 114793 (2022).

38. Raducan, S. D. et al. Influence of the projectile geometry on the momentum transfer from a kinetic impactor and implications for the DART mission. *Int. J. Impact Eng.* **162**, 104147 (2022).

39. Owen, J. M., DeCoster, M. E., Graninger, D. M. & Raducan, S. D. Spacecraft geometry effects on kinetic impactor missions. *Planet. Sci. J.* **3**, 218 (2022).

40. Holsapple, K. A. & Housen, K. R. A crater and its ejecta: an interpretation of Deep Impact. *Icarus* **191**, 586–597 (2007).

41. Ernst, C. M. et al. Characterization of the DART impact site on Dimorphos. In *Proc. 54th Lunar and Planetary Science Conference* 2529 (LPI, 2023).

42. Pravec, P. et al. Binary asteroid population. 3. Secondary rotations and elongations. *Icarus* **267**, 267–295 (2016).

43. Nakano, R. et al. NASA's Double Asteroid Redirection Test (DART): mutual orbital period change due to reshaping in the near-Earth binary asteroid system (65803) Didymos. *Planet. Sci. J.* **3**, 148 (2022).

44. Agrusa, H. F. et al. The excited spin state of Dimorphos resulting from the DART impact. *Icarus* **370**, 114624 (2021).

45. Richardson, D. C. et al. Predictions for the dynamical states of the Didymos system before and after the planned DART impact. *Planet. Sci. J.* **3**, 157 (2022).

46. Tricarico, P. et al. Internal rubble properties of asteroid (101955) Bennu. *Icarus* **370**, 114665 (2021).

47. Fujiwara, A. et al. The rubble-pile asteroid Itokawa as observed by Hayabusa. *Science* **312**, 1330–1334 (2006).

48. Zhang, Y. et al. Creep stability of the DART/Hera mission target 65803 Didymos: II. The role of cohesion. *Icarus* **362**, 114433 (2021).

49. Scheeres, D. J., Hartzell, C. M., Sanchez, P. & Swift, M. Scaling forces to asteroid surfaces: the role of cohesion. *Icarus* **210**, 968–984 (2010).

50. Ferrari, F. & Tanga, P. Interior of top-shaped asteroids with cohesionless surface. *Icarus* **378**, 114914 (2022).

51. Walsh, K. J., Richardson, D. C. & Michel, P. Rotational breakup as the origin of small binary asteroids. *Nature* **454**, 188–191 (2008).

52. Ferrari, F., Raducan, S. D., Soldini, S. & Jutzi, M. Ejecta formation, early collisional processes, and dynamical evolution after the DART impact on Dimorphos. *Planet. Sci. J.* **3**, 177 (2022).

53. Arakawa, M. et al. An artificial impact on the asteroid (162173) Ryugu formed a crater in the gravity-dominated regime. *Science* **368**, 67–71 (2020).

54. Walsh, K. J. et al. Near-zero cohesion and loose packing of Bennu's near subsurface revealed by spacecraft contact. *Sci. Adv.* **8**, eabm6229 (2022).

55. Barnouin, O. S. et al. The formation of terraces on asteroid (101955) Bennu. *J. Geophys. Res. Planets* **127**, e2021JE006927 (2022).

56. Zhang, Y. et al. Creep stability of the proposed AIDA mission target 65803 Didymos: I. Discrete cohesionless granular physics model. *Icarus* **294**, 98–123 (2017).

57. Weibull, W. A statistical distribution function of wide applicability. *J. Appl. Mech.* **18**, 293–297 (1951).

58. Brown, W. K. & Wohletz, K. H. Derivation of the Weibull distribution based on physical principles and its connection to the Rosin–Rammler and lognormal distributions. *J. Appl. Phys.* **78**, 2758–2763 (1995).

59. Robin, C. Q. et al. A comparative study of boulder morphology on small body surfaces. In *Proc. Asteroids, Comets, Meteors Conference* 2851 (LPI, 2023).

60. Benz, W. & Asphaug, E. Simulations of brittle solids using smooth particle hydrodynamics. *Comput. Phys. Commun.* **87**, 253–265 (1995).

61. Benz, W. & Asphaug, E. Catastrophic disruptions revisited. *Icarus* **142**, 5–20 (1999).

62. Nyffeler, B. *Modelling of Impacts in the Solar System on a Beowulf Cluster*. PhD thesis, Univ. of Bern (2004).

63. Jutzi, M., Michel, P., Hiraoka, K., Nakamura, A. M. & Benz, W. Numerical simulations of impacts involving porous bodies: II. Comparison with laboratory experiments. *Icarus* **201**, 802–813 (2009).

64. Luther, R. et al. Momentum enhancement during kinetic impacts in the low-intermediate-strength regime: benchmarking and validation of impact shock physics codes. *Planet. Sci. J.* **3**, 227 (2022).

65. Richardson, D. C., Quinn, T., Stadel, J. & Lake, G. Direct large-scale *N*-body simulations of planetesimal dynamics. *Icarus* **143**, 45–59 (2000).

66. Tillotson, H. J. *Metallic Equations of State for Hypervelocity Impact*. Report No. GA-3216 (General Atomic, 1962).

67. Collins, G. S., Kenkmann, T., Osinski, G. R. & Wünnemann, K. Mid-sized complex crater formation in mixed crystalline-sedimentary targets: insight from modeling and observation. *Meteorit. Planet. Sci.* **43**, 1955–1977 (2008).

68. Chourey, S., Koschny, D., Rott, M. & Schmausser, C. Determining the momentum transfer in regolith-like targets using the TUM/LRT electro-thermal accelerator. *Planet. Space Sci.* **194**, 105112 (2020).

69. León, J. D., Licandro, J., Serra-Ricart, M., Pinilla-Alonso, N. & Campins, H. Observations, compositional, and physical characterization of near-Earth and Mars-crosser asteroids from a spectroscopic survey. *Astron. Astrophys.* **517**, A23 (2010).

70. Consolmagno, G. J., Britt, D. T. & Macke, R. J. The significance of meteorite density and porosity. *Geochemistry* **68**, 1–29 (2008).

71. Britt, D. T. & Consolmagno, G. J. S. J. Stony meteorite porosities and densities: a review of the data through 2001. *Meteorit. Planet. Sci.* **38**, 1161–1180 (2003).

72. Herrmann, W. Constitutive equation for the dynamic compaction of ductile porous materials. *J. Appl. Phys.* **40**, 2490–2499 (1969).

73. Carroll, M. & Holt, A. C. Suggested modification of the P–α model for porous materials. *J. Appl. Phys.* **43**, 759–761 (1972).

74. Hagerty, M. M., Hite, D. R., Ullrich, C. R. & Hagerty, D. J. One-dimensional high-pressure compression of granular media. *J. Geotech. Eng.* **119**, 1–18 (1993).

75. Housen, K. R., Sweet, W. J. & Holsapple, K. A. Impacts into porous asteroids. *Icarus* **300**, 72–96 (2018).

76. Stephens, D. R. & Lilley, E. M. Compressibilities of lunar crystalline rock, microbreccia, and fines to 40 kilobars. *Science* **167**, 731–732 (1970).

77. Ahrens, T. J. & Cole, D. M. Shock compression and adiabatic release of lunar fines from Apollo 17. *Lunar Planet. Sci. Conf. Proc.* **3**, 2333 (1974).

78. Nakamura, A. M., Hiraoka, K., Yamashita, Y. & Machii, N. Collisional disruption experiments of porous targets. *Planet. Space Sci.* **57**, 111–118 (2009).

79. Jutzi, M. & Michel, P. Hypervelocity impacts on asteroids and momentum transfer. I. Numerical simulations using porous targets. *Icarus* **229**, 247–253 (2014).

80. Stickle, A. M. et al. Modeling momentum transfer from kinetic impacts: implications for redirecting asteroids. *Procedia Eng.* **103**, 577–584 (2015).

Acknowledgements

Author contributions

S.D.R., M.J. and A.F.C. conceptualized the study. S.D.R. ran the simulations and analysed the data. S.D.R., M.J., A.F.C., O.B. and G.S.C. wrote the initial draft. Y.Z. provided the rubble-pile models. R.T.D., C.M.E. and O.B. provided the shape model of Dimorphos. T.L.F. provided the viewing geometry for comparison with LICIACube data. M.H., J.Y.L. and P.H.H. provided measurements of the ejecta. Y.Z., F.F. and H.F.A. helped with interpreting the results. R.N. helped with understanding the effects of deformation on the dynamics. M.P., A.L. and F.T. provided boulder SFDs. C.Q.R. and N.M. provided the boulder shapes. A.F.C., H.F.A. and B.W.B. provided momentum-enhancement measurements. A.R., E.D. and P.H.H. provided LICIACube measurements. P.P. provided observational inputs. P.S. helped with interpreting the cohesion. T.M.D., K.M.K., P.M., M.B.S., N.L.C., E.D., E.G.F., I.H., S.I., R.L., J.O., M.O., A.S.R., K.W., A.Z. and E.M.E. provided comments that substantively revised the manuscript. C.M. and B.H.M. provided the stereographs of the Didymos system.

Funding

Competing interests

The authors declare no competing interests.

Additional information

Extended data Extended data are available for this paper at https://doi.org/10.1038/s41550-024-02200-3.

Supplementary information The online version contains supplementary material available at https://doi.org/10.1038/s41550-024-02200-3.

Correspondence and requests for materials should be addressed to S. D. Raducan.

Peer review information *Nature Astronomy* thanks the anonymous reviewers for their contribution to the peer review of this work.

Reprints and permissions information is available at www.nature.com/reprints.

Publisher's note Springer Nature remains neutral with regard to jurisdictional claims in published maps and institutional affiliations.

[1]Space Research and Planetary Sciences, Physics Institute, University of Bern, Bern, Switzerland. [2]Johns Hopkins University Applied Physics Laboratory, Laurel, MD, USA. [3]Department of Aerospace Engineering, University of Maryland, College Park, MD, USA. [4]Department of Earth Science and Engineering, Imperial College London, London, UK. [5]Department of Aerospace Science and Technology, Politecnico di Milano, Milan, Italy. [6]Guggenheim School of Aerospace Engineering, Georgia Institute of Technology, Atlanta, GA, USA. [7]Department of Aerospace Engineering, Auburn University, Auburn, AL, USA. [8]Lawrence Livermore National Laboratory, Livermore, CA, USA. [9]Université Côte dAzur, Observatoire de la Côte dAzur, CNRS, Laboratoire Lagrange, Nice, France. [10]University of Tokyo, Department of Systems Innovation, School of Engineering, Tokyo, Japan. [11]Institut Supérieur de l'Aéronautique et de l'Espace (ISAE-SUPAERO), Université de Toulouse, Toulouse, France. [12]INAF-OAPD Astronomical Observatory of Padova, Padua, Italy. [13]IFAC-CNR, Sesto Fiorentino (FI), Italy. [14]NASA/Goddard Space Flight Center, Greenbelt, MD, USA. [15]INAF-Osservatorio Astronomico di Roma, Rome, Italy. [16]Jet Propulsion Laboratory, California Institute of Technology, Pasadena, CA, USA. [17]Centro de Astrobiología (CAB), CSIC-INTA, Torrejón de Ardoz, Spain. [18]INAF-Osservatorio Astronomico di Trieste, Trieste, Italy. [19]Planetary Science Institute, Tucson, AZ, USA. [20]Museum für Naturkunde, Leibniz Institute for Evolution and Biodiversity Science, Berlin, Germany. [21]Astronomical Institute of the Czech Academy of Sciences, Ondřejov, Czech Republic. [22]Colorado Center for Astrodynamics Research, University of Colorado Boulder, Boulder, CO, USA. [23]Agenzia Spaziale Italiana; ASI Space Science Data Center, Rome, Italy. [24]London Stereoscopic Company, London, UK. ✉e-mail: sabina.raducan@unibe.ch
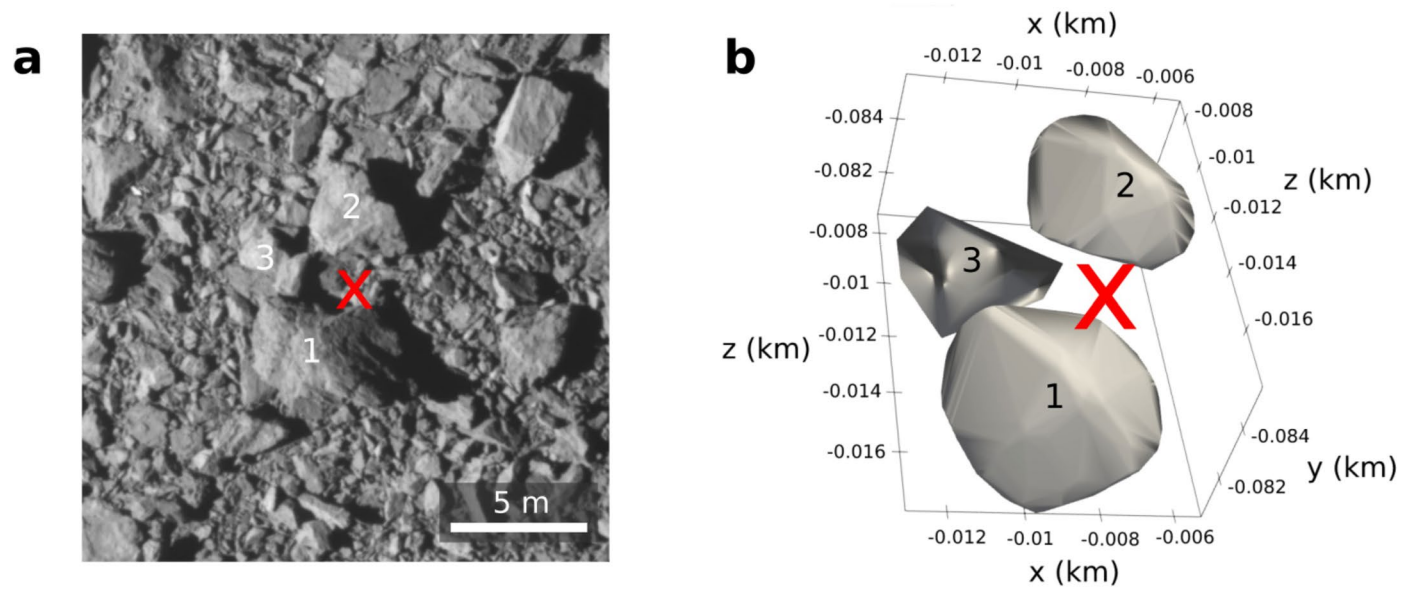
Extended Data Fig. 1 | Impact location. (a) Excerpt of the final full DRACO image of Dimorphos's surface (*dart_0401930049_43695_01_iof.fits*), ~2 s before impact[1]. The red x indicates the approximate impact location. The north pole of Dimorphos is toward the top of the figure. (b) Convex hulls of the boulders at the impact location extracted from the impact site DTM[1].
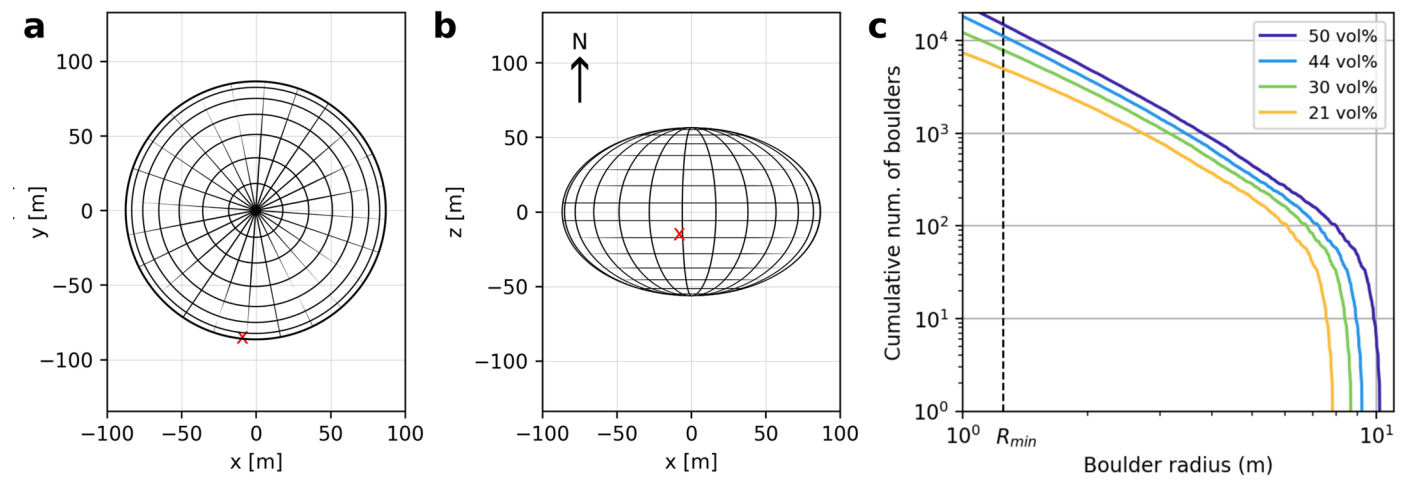
Extended Data Fig. 2 | Dimorphos shape and boulders SFD. (a, b) Oblate ellipsoid shape of the target, with X: 177 m; Y: 174 m and Z: 116 m. The red cross at 8.84 +/- 0.4 deg S, 264.30 +/− 0.47 deg E (x ∼ − 8.31, z ∼ − 12.69 m) shows the impact location. (c) Boulder SFDs used in this study, with ∼ 21, 30, 44 and 50% volume fractions.
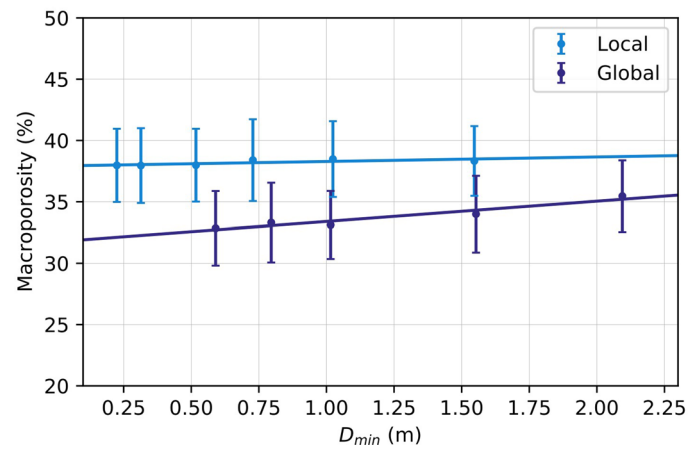
Extended Data Fig. 3 | Macroporosity calculations from the local and the global boulder SFD on Dimorphos, as a function of assumed minimum boulder size, D_{min}**.** We find 38 +/- 3% macroporosity from the local SFD and 34 +/- 4% from the global SFD (1-sigma uncertainty). Macroporosity calculations from the local and the global boulder SFD on Dimorphos, as a function of assumed minimum boulder size, D_{min}. We find 38 +/- 3% macroporosity from the local SFD and 34 +/- 4% from the global SFD (1-sigma uncertainty).

a Cumulative number per km² vs Size (m); Weibull: $N(D) = N_T \exp(-3(D/\lambda))^{\beta}/\beta$
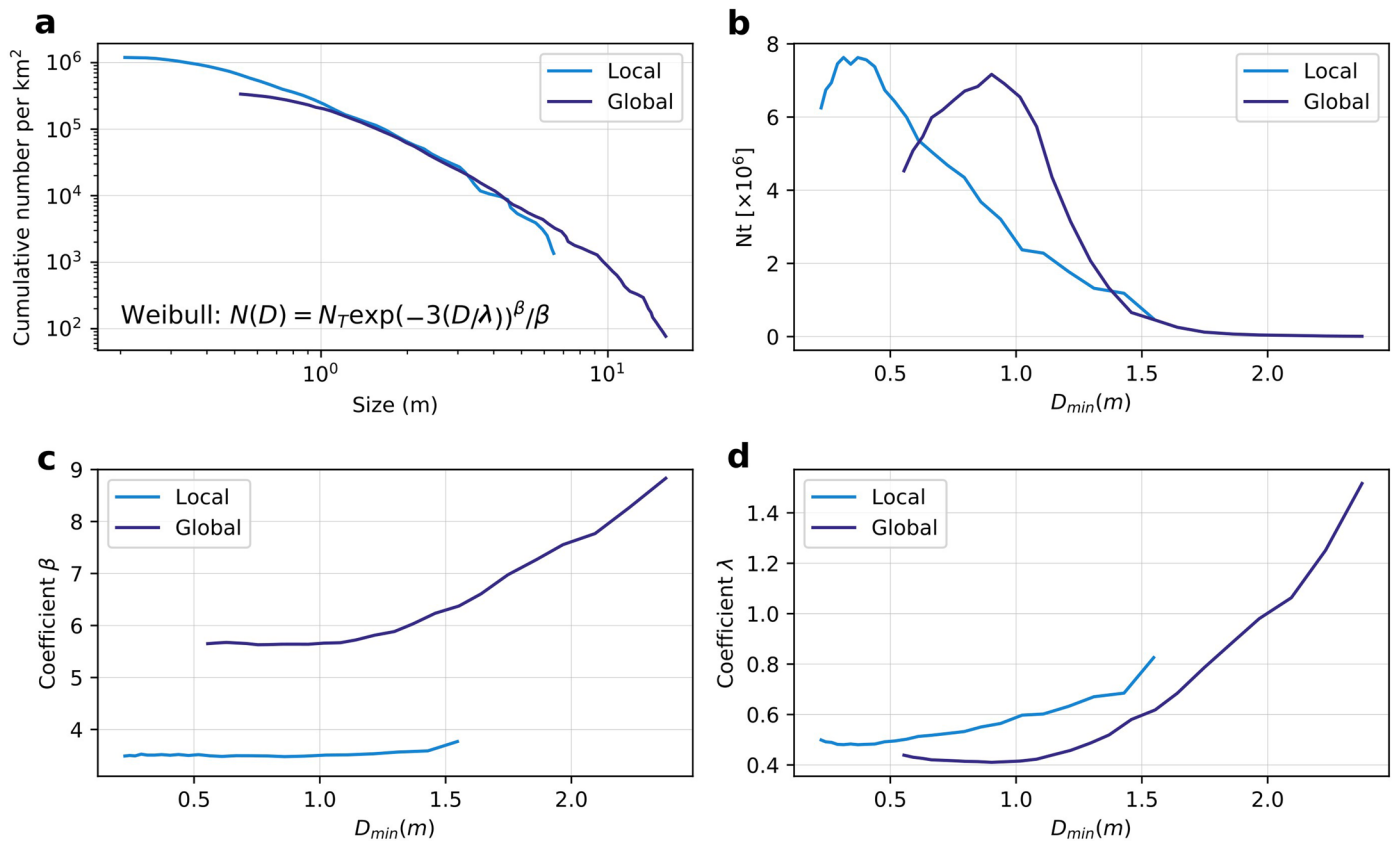
Extended Data Fig. 4 | Boulders size-frequency distribution and Weibull parameters. (a) Cumulative number of boulders per km² as a function of size as counted in the final complete image from the DART spacecraft, which includes the impact site[1] and on the illuminated side of Dimorphos[19]. (b), (c), (d) Weibull parameters derived by fitting Eq. (2) to the local and global SFDs.
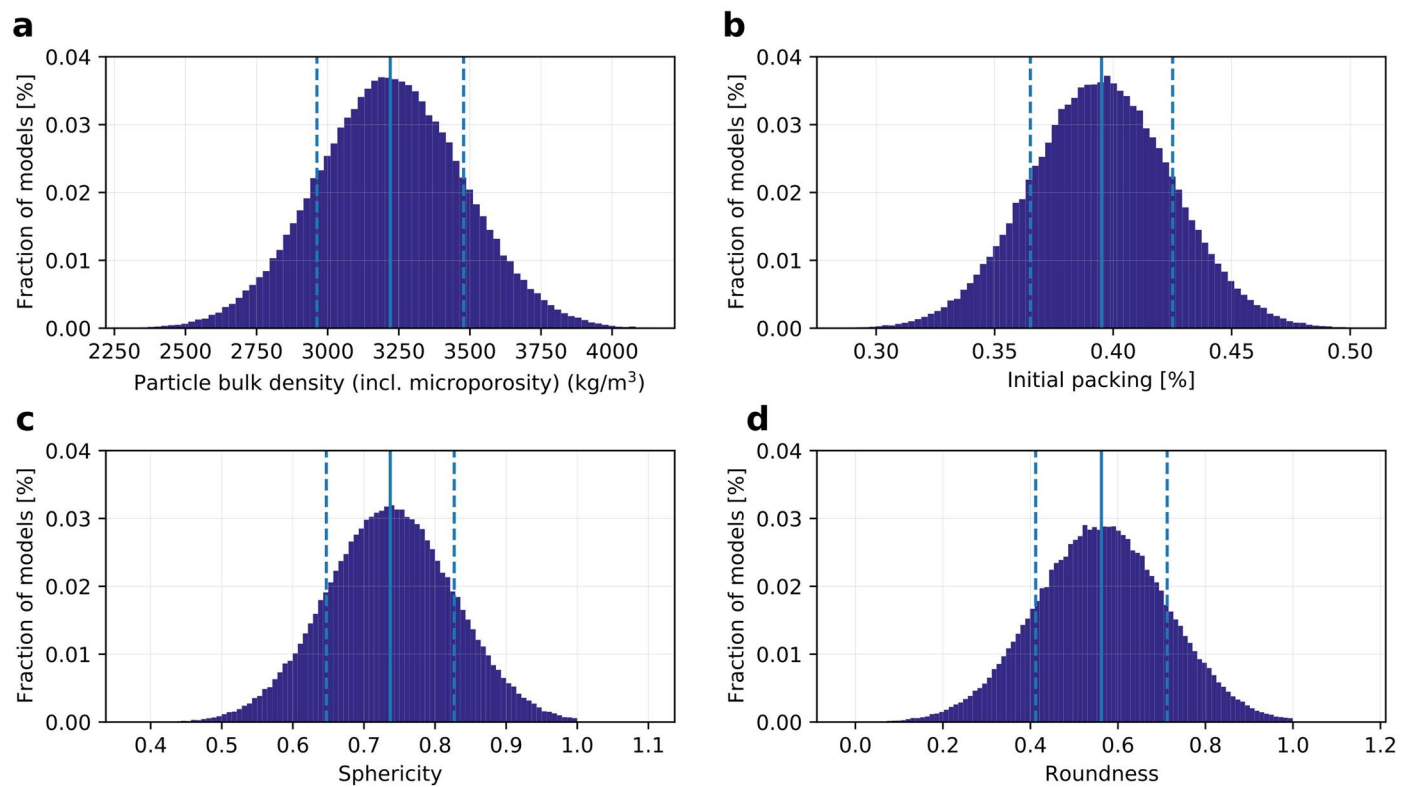
Extended Data Fig. 5 | Histograms of particle bulk density, initial packing, sphericity and roundness obtained using Monte-Carlo simulations. Histograms of (a) Particle bulk density, (b) Initial packing, (c) Sphericity and (d) Roundness obtained using Monte-Carlo simulations. The Gaussian distributions of sphericity and roundness are cut at 1.
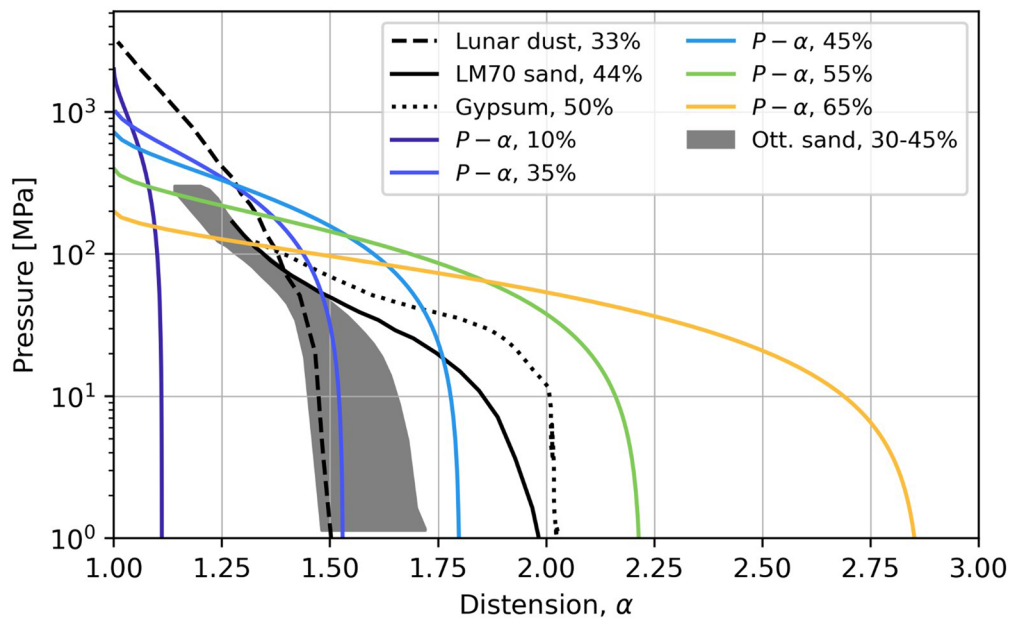
Extended Data Fig. 6 | Crush curves. Crush curves (distension, alpha, versus pressure) used in Bern SPH for boulders (10% porosity) and for the matrix material (35-65% porosity), compared with experimentally derived quasi-static crush curves for lunar dust[76], gypsum[78], Lane Mtn. #70 sand[75] and Ottawa sand (shaded area)[74].
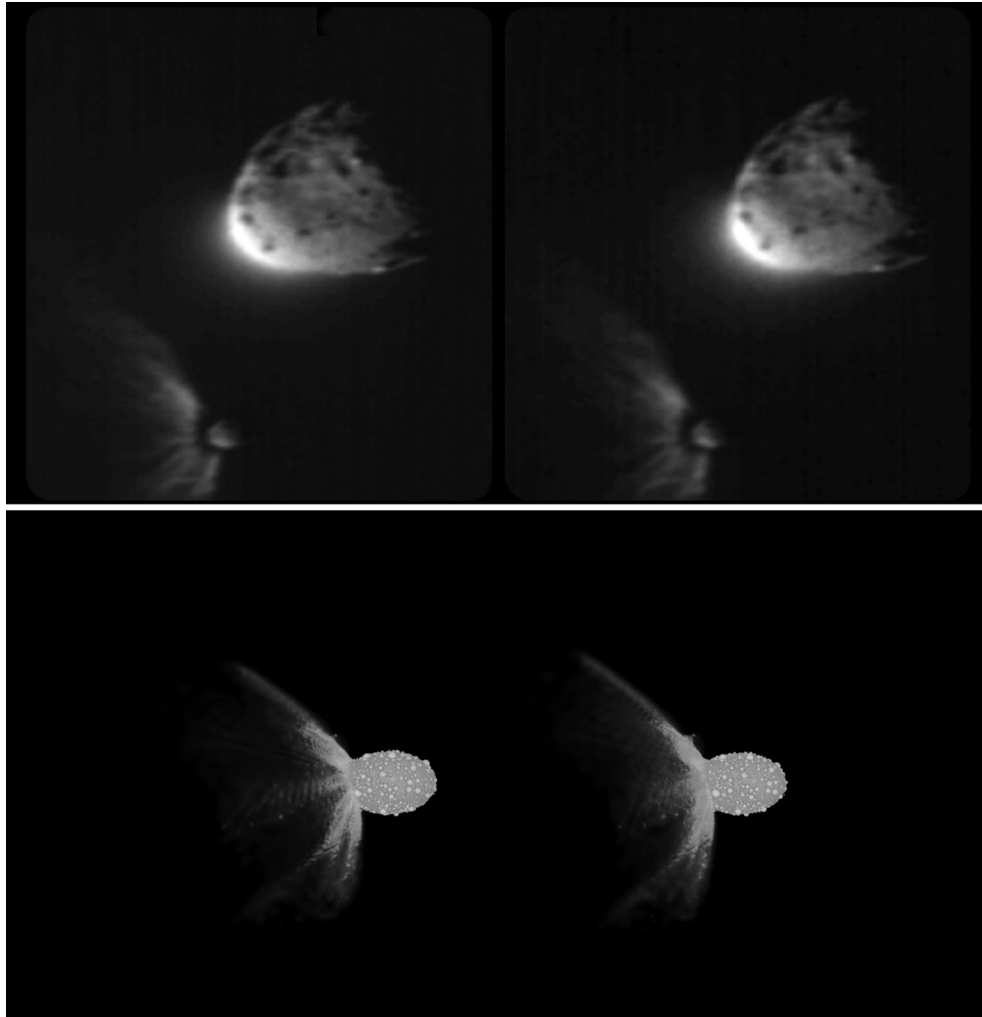
Extended Data Fig. 7 | Stereoscopic pair from LICIACube images of the Didymos system and from Bern SPH simulations at T ~ 178 s. These stereoscopic pairs can be viewed in "parallel" stereo mode simply by relaxing the eye convergence. We suggest viewing the pair of images from a foot or so away, and look through the screen to infinity, allowing the two images to float across each other. Where the two central pictures exactly overlap, the "fused" 3-D image is to be found; all that is then necessary is to gently adjust the focus of the eyes, while the convergence remains relaxed, to obtain a clear stereoscopic image. This technique is called 'Free Viewing' of stereo pairs. For a more authentic stereo effect, use a Brewster format stereoscope - The London Stereoscopic Company OWL or similar. Detailed instructions may be found at LondonStereo.com.

Extended Data Table 1 | DART input constraints

Source	Parameter	Values	Reference
Impact conditions			
	Spacecraft mass	579.4 ± 0.7 kg	[1]
	Impact speed	6.1449 ± 0.0003 km/s	[1]
	Impact velocity	(-1.06, 5.96, 1.03) km/s	[1]
	Impact angle	17 ± 7 from the surface normal	[1]
	Impact site lat/lon	$8.84 \pm 0.45°$ S, $264.30 \pm 0.47°$ E	[1]
Dimorphos characterisation			
	Extent of Dimorphos	177 ± 2; 174 ± 4; 116 ± 2 m	[1]
	Volume	$0.00181 \pm 10\%$ km^3	[1]
	Angle of friction from surface slope	$<30°$	[41]
	Global boulder SFD	Extended data Fig. 4	[19]
	Didymos/Dimorphos spectral type	S-type	[22, 76]
	Didymos/Dimorphos meteorite analogues	L/LL chondrites	[20, 21]
	L/LL chondrites grain density	3200–3600 kg/m^3	[23, 77]
	L/LL chondrites microporosity	8–10%	[23, 78]
	Boulder strength	10 MPa	see Methods
	Global macroporosity	$34 \pm 4\%$	see Methods
Impact site characterisation			
	Local boulders SFD	Extended data Fig. 4	[1]
	Boulders sphericity	0.74 ± 0.25	[79]
	Boulders roundness	0.56 ± 0.44	[79]
	Macroporosity	$38 \pm 3\%$	see Methods

Observations and DART input constraints.

Extended Data Table 2 | Material model parameters for impact simulations into Dimorphos analogues

Description	Impactor	Matrix material	Boulders
Material	Aluminium	Basalt	Basalt
Equation of state	Tillotson[a]	Tillotson[b]	Tillotson[b]
Grain density, ρ_g (kg/m^3)	1000	3200/3500	3200/3500
Strength model	von Mises	LUND[c]	LUND[c]
LUND strength parameters[c]			
Damage strength at zero pressure, Y_0 (Pa)	–	0–500	1×10^8
Strength at infinite pressure, Y_{inf} (GPa)	0.34	3.5	3.5
Internal friction coefficient (damaged), f	–	0.4/0.55/0.7	0.8
Porosity model parameters $(P-\alpha)^d$			
Initial porosity, ϕ_0	–	35–65%	10%
Initial distension, α_0	–	1.53–2.87	1.15
P_s (MPa)	–	1100–200	2000
P_e (MPa)	–	1.0	1.0
n	–	2	2

[a][80]; [b][60]; [c][25]; [d][14].

Extended Data Table 3 | Observational constraints

Source	Parameter	Values	Reference
Ejecta plume morphology			
	Cone opening angle from HST, ω	$125° \pm 10°$	[5]
	Cone opening angle LICIA, ω	$135° \pm 4°$	[4]
	Cone direction HST solution 1 (RA, DEC)	$141 \pm 8°$, $25 \pm 6°$	[5]
	Cone direction HST solution 2 (RA, DEC)	$120 \pm 9°$, $10 \pm 7°$	[5]
	Cone direction LICIACube (RA, DEC)	$137 \pm 9°$, $19 \pm 12°$	[4]
	Cone direction HST & LICIACube (RA, DEC)	$138 \pm 15°$, $13 \pm 15°$	[7]
	Ejecta mass, M_{ej}	more than 1.3–2.2×10^7 kg	[6]
Deflection efficiency			
	Pre-impact orbit period (P_{pre})	11 hours 55 minutes	[2]
	Post-impact orbit period (P_{post})	11 hours 23 minutes	[2]
	Period change, ΔP	33.0 ± 1.0 (3σ) minutes	[2]
	Along-track velocity change, Δv_T	-2.7 ± 0.10 (1σ) mm/s	[7]
	Momentum enhancement, β	$(3.61 \pm 0.20) \times \frac{\rho_B}{2400 kg/m^3}$	[7]

Observational constrains. Here we provide a summary of the constraints derived from observations, the DRACO camera and meteorite analogues. (HST = Hubble Space Telescope observations[5]; LICIACube = LICIACube observations[4]).